

UC Berkeley

UC Berkeley Previously Published Works

Title

Influence of Si on the Microstructure and Mechanical and Tribological Properties of Ag/a-C:H Films

Permalink

<https://escholarship.org/uc/item/5zh462q1>

Journal

Tribology transactions, 63(5)

ISSN

1040-2004

Authors

Wu, Yanxia
Zhang, Shujiao
Meng, Jie
[et al.](#)

Publication Date

2020-09-02


DOI

10.1080/10402004.2020.1773593

Peer reviewed



Influence of Si on the Microstructure and Mechanical and Tribological Properties of Ag/*a*-C:H Films

Yanxia Wu^a, Shujiao Zhang^a, Jie Meng^a, Shengxi Wang^b, Shengwang Yu^a, Yong Ma^a, Bin Tang^a, Ying Liu^a, and Kyriakos Komvopoulos^b 

^aInstitute of New Carbon Materials, Taiyuan University of Technology, Taiyuan, P. R. China; ^bDepartment of Mechanical Engineering, University of California, Berkeley, CA, USA

ABSTRACT

The relatively high toughness, high adhesion to steel, and low internal stress of hydrogenated amorphous carbon (*a*-C:H) films containing Ag make them good candidate materials for various applications in sensors, tribology, and biomaterials; however, the relatively low hardness and poor tribological properties in oxidizing environments hinder their broad use. Incorporating a small amount of Si in Ag/*a*-C:H films may modify the film microstructure and, in turn, improve their mechanical and tribological properties. To test this hypothesis, Ag/Si/*a*-C:H films were synthesized by magnetron sputtering and their microstructure, composition, and mechanical/tribological properties were examined with various microanalysis techniques and mechanical testing methods. The Si content of the films was varied by controlling the rotational speed of the substrate. It is shown that the incorporation of Si in the films increases the sp^3 C, sp^3 CH, and sp^3 CH₂ contents, slightly roughens the film surface, and greatly improves the mechanical and tribological properties through the formation of a SiC phase. The results of this study also show that there is a critical Si content for optimal tribological properties.

ARTICLE HISTORY

Received 3 October 2019
Accepted 19 May 2020

KEYWORDS

Hydrogenated amorphous carbon; composition; films; mechanical/tribological properties; silicon; silver

Introduction

With increasing demands for high reliability and efficiency of contact-mode electrical and mechanical components, preserving the integrity of contact interfaces subjected to various loadings and operation conditions is of critical importance. Hydrogenated amorphous carbon (*a*-C:H) films are commonly used as protective overcoats due to their unique physical properties, such as high hardness, good wear resistance, and chemical inertness. Typically, *a*-C:H films possess structures consisting of various atomic hybridizations, such as tetrahedral (sp^3), trigonal (sp^2), and linear (sp^1) carbon atom bonding (1). The *a*-C:H film properties greatly depend on the hydrogen content and carbon hybridization. The tribological properties of *a*-C:H films with low hydrogen and sp^3 contents are similar to those of graphite, exhibiting low friction and high wear resistance in reactive (e.g., O₂ and air) atmospheres but high friction and low wear resistance in inert atmospheres (e.g., N₂ and vacuum), whereas *a*-C:H films with high hydrogen and sp^3 contents show an opposite trend (2). A plausible solution to this problem is the development of composite films that contain other elements (3, 4). Film with single-metal doping can lower the internal stress by converting the strong carbon-carbon bonds to weaker metal-carbon bonds and form metal nanocrystallites that cause structure relaxation (5). Unfortunately, metal doping usually degrades the mechanical

and/or tribological properties of the film (6, 7). For example, whereas Ag/*a*-C:H films demonstrate low internal stress, high toughness, and low friction in vacuum (8) and biological fluid environments (9), the structural changes at the film surface due to the aggregation of Ag (10, 11) decrease the film hardness and, in the presence of oxidative agents and water vapor, promote hydrocarbon adsorption and oxidation (12) and aging (13), which can have detrimental effects on the tribological properties of Ag/*a*-C:H films. This problem can be overcome by multi-element film doping (14, 15). For example, Ti and Al co-doping of *a*-C:H films lowers the residual stress, enhances the toughness, and improves the tribological properties (16, 17). This provides impetus for exploring the incorporation of other elements into Ag/*a*-C:H films that can improve the tribological properties in air while maintaining relatively high hardness and low internal stress.

A promising element for doping *a*-C:H films is Si, because it can increase the sp^3 content and improve the mechanical properties, corrosion resistance, and interfacial adhesion to various substrates. The reaction of Si incorporated in *a*-C:H films with hydroxides in solution can be beneficial to the tribological properties of the film (18). Moreover, Si may promote osteoblast proliferation and bone restructuring in biological environments, improving the biological properties of *a*-C:H films (19). It has also been reported that incorporating Si and Ag in *a*-C:H films

enhances the bacterial activity and biocompatibility (20–23). However, basic knowledge of the tribological behavior of these films in reactive atmospheres is sparse and empirical. Therefore, fundamental insight into the effects of composition and microstructure on the mechanical and tribological properties of Si/Ag/*a*-C:H nanocomposite films is of particular interest. The main objective of this study was to perform a comprehensive analysis of the microstructure, composition, surface morphology, and mechanical and tribological properties of Si/Ag/*a*-C:H films with varying Si contents synthesized by magnetron sputtering. Results from various microanalysis studies, nanoindentation tests, and sliding experiments are presented to elucidate the effect of Si content on the film microstructure and mechanical/tribological properties.

Experimental methods

Film deposition

Deposition of Si/Ag/*a*-C:H films on p-type Si (111) and 304 stainless steel substrates, which were previously cleaned with acetone in air, was performed by magnetron sputtering. Ar and CH₄ gases of 99.99% purity and different flow rates were used as sputtering and reactive gases, respectively. Two circular targets consisting of Si and graphite/Ag (10:1 in volume) were used in the film deposition experiments. The Si target was connected to a medium-frequency pulsed DC power supply operated at 80 W and 80% duty cycle, and the graphite/Ag target was connected to an RF power supply operated at 150 W. The substrates were first rinsed with acetone and then cleaned further in the chamber with Ar plasma. Ar gas was introduced into the chamber and maintained at a pressure of 1.5×10^{-2} Pa and a Kaufman ion source with a 5-cm-wide beam was turned on for 10 min to remove the native oxide film and any airborne adsorbents on the substrate surface. An ~200-nm-thick Si layer was then deposited on the substrate by sputtering the Si target with Ar⁺ ions (DC power = 80 W; chamber pressure = 0.7 Pa; duration = 40 min) to improve the adhesion between the substrate and the *a*-C:H film (24). After this step, Si/Ag/*a*-C:H film deposition onto the Si-coated substrates was performed by sputtering both targets with Ar and CH₄ plasmas (RF power = 150 W [graphite/Ag target]; DC power = 80 W [Si target]; chamber pressure = 0.7 Pa; Ar gas flow rate = 40 sccm; CH₄ gas flow rate = 20 sccm). The substrate bias voltage during film deposition was set at 110 V. To vary the Si content of the films, the substrate was continuously rotated during film deposition. Hereafter, the Si/Ag/*a*-C:H films synthesized at substrate rotational speeds of 5, 3, and 1 rpm will be denoted as A2, A3, and A4, respectively. The distance between the substrate and target during a rotation varied from 10 to 26 cm; the distance between the substrate and the target was the nearest (10 cm) when the substrate rotated face on, and the distance was the furthest (26 cm) when the substrate rotated far from this target face to the other one. The substrate rotated in a circular track with a diameter of 16 cm. The distances between the substrate and each target were the same when deposition

was stopped. An Ag/*a*-C:H film (denoted as A1) deposited under the same deposition conditions as the Si/Ag/*a*-C:H films, except for the sputtering power of the Si target that was set equal to zero, was used as the control. The total deposition time was 3 h. The resulting film thickness (measured with a 3D noncontact profilometer) was found to be equal to $1.6 \pm 0.1 \mu\text{m}$ (the thickness of the A1, A2, A3, and A4 films was equal to 1.57, 1.59, 1.60, 1.62 μm , respectively).

Microanalysis and testing methods

The chemical composition and binding state of the nanocomposite films were examined by X-ray photoelectron spectroscopy (XPS), with Al-K α radiation (photon energy = 1,476.6 eV) as the excitation source. The type of carbon bonding was examined with a Raman spectrometer using an excitation wavelength of 532 nm (2.34 eV). Fourier transform infrared (FTIR) spectra were obtained in the wavenumber range of 400–4000 cm⁻¹. The crystallographic structure and surface morphology of the films were examined by X-ray diffraction (XRD) using a grazing incident angle fixed at 2° and an atomic force microscope (AFM) operated in noncontact dynamic mode, respectively. The surface roughness of the films was measured at least three times for every sample with an area of $3 \times 3 \mu\text{m}^2$. The variation in the measurement for A1, A2, A3, and A4 samples was found equal to ± 0.05 , ± 0.07 , ± 0.06 , and ± 0.09 , respectively. The root-mean-square (RMS) roughness of the sample nearest to the average value was chosen for comparison.

The mechanical properties (i.e., hardness and elastic modulus) of the films were evaluated with a nanoindenter using a 50-nm-radius Berkovich diamond tip and maximum indentation load of 2.2 N. To avoid a substrate effect on the measurements, the maximum indentation depth was set to <10% of the film thickness. Under these testing conditions, the maximum indentation depth was found to be ~90 nm. The tribological characteristics of the films were studied with a reciprocating ball-on-disc tribometer using a normal load of 2 N; oscillation frequency and amplitude equal to 2 Hz and 5 mm, respectively; and 30 min total sliding time. The tribological tests were performed three times for every sample at room temperature and 45% relative humidity. The counterspecimen was a 5-mm-diameter GCr15 steel ball (96.4 Fe, 0.95–1.05 C, 0.25–0.45 Mn, 0.025 P, 0.02 S, 1.40–1.65 Cr, 0.25 Cu, and 0.25 Ni, all vol%). The worn surfaces on the films and the steel balls were observed with a scanning electron microscope (SEM), operated at an acceleration voltage of 20 kV, which was equipped with an energy-dispersive spectrometer. The wear rate was calculated using the formula: $k = V/(F \times S)$, where k is the wear rate, V is the wear volume (mm³), F is the normal load (N), and S is the sliding distance (m).

Results and discussion

Film composition and structure

The chemical composition and microstructure of the synthesized films were analyzed by XPS. Table 1 shows the effect

of the substrate rotational speed on film chemical composition. It is noted that the Si content increased and the C content decreased with the decrease of the rotational speed without affecting the Ag content. This is attributed to the growth of different particles at the film surface. Though the amount and energy of particles generated from the decomposition of CH_4 were constant during film deposition, the amount and energy of the particles that were sputtered off from the targets decreased with increasing target–substrate distance during the rotation of the substrate. High-energy particles are more likely to be implanted in the growing film and react with other particles, whereas low-energy particles are usually weakly bonded with surface atoms and therefore more likely to be sputtered off subsequently by other impinging particles. Because of the larger mass of Ag particles, it was more difficult for these particles to be sputtered off from the growing film surface by other lighter particles. Therefore, the Ag content was not affected by the rotational speed of the substrate. Alternatively, the lighter Si and C particles were easily sputtered off during deposition, showing opposite trends with decreasing rotational speed. More Si particles deposited on the growing film surface with

decreasing rotational speed due to the increase in substrate dwell time under the Si target. The energetic Si particles penetrated and disrupted the C network, reacting with C atoms to form Si-rich regions (as shown by XPS results), increasing the Si content of the Si/Ag/a-C:H films. The greater etching resistance of the Si-rich regions compared to C regions is responsible for the increase in Si content and the decrease in C content with decreasing rotational speed of the substrate; that is, increasing substrate dwell time under each target.

The film composition was determined from XPS analysis using Al-K α radiation (photon energy = 1,476.6 eV, chamber pressure of $<10^{-8}$ Torr) as the excitation source. Calculation of atom concentrations corresponding to the Si 2p, Ag 3d, Au 4f, and C 1s core levels was based on the standard sensitivity factors of the instrument. Each sample was sputter coated with an Au film and the Au 4f spectrum was used for charge calibration of the XPS spectra. Fine spectra of C 1s, Ag 3d, and Si 2p core-level peaks are shown in Figs. 1a–1d, 1e, and 1f, respectively. The C 1s peaks were fitted with Gaussian distributions centered at 283.7, 284.5, 285.4, 286.5, and 287.8 eV corresponding to Si-C, sp^2 C, sp^3 C-C and C-H, C-O, and O-C=O bonds, respectively. The C-O and O-C=O bonds are attributed to physisorption of O from the air and chamber wall. The dominance of the distribution centered at ~ 284.5 eV indicates that all films were rich in sp^2 C=C bonding. The intensity of the Si-C peak increased with the Si content. The spectra shown in Fig. 1e contain two characteristic peaks centered at 367.6 and 373.6 eV that are assigned to Ag 3d $_{5/2}$ and Ag 3d $_{3/2}$, respectively. The close similarity of the Ag 3d spectra

Table 1. Chemical composition of composite A1–A4 films deposited at different rotational speeds.

Si/Ag/a-C:H film	Substrate rotational speed (rpm)	Film composition (at%)		
		C	Ag	Si
A1	5	94.16	5.84	0
A2	5	89.72	5.86	4.42
A3	3	85.85	5.95	8.20
A4	1	83.26	5.76	10.98

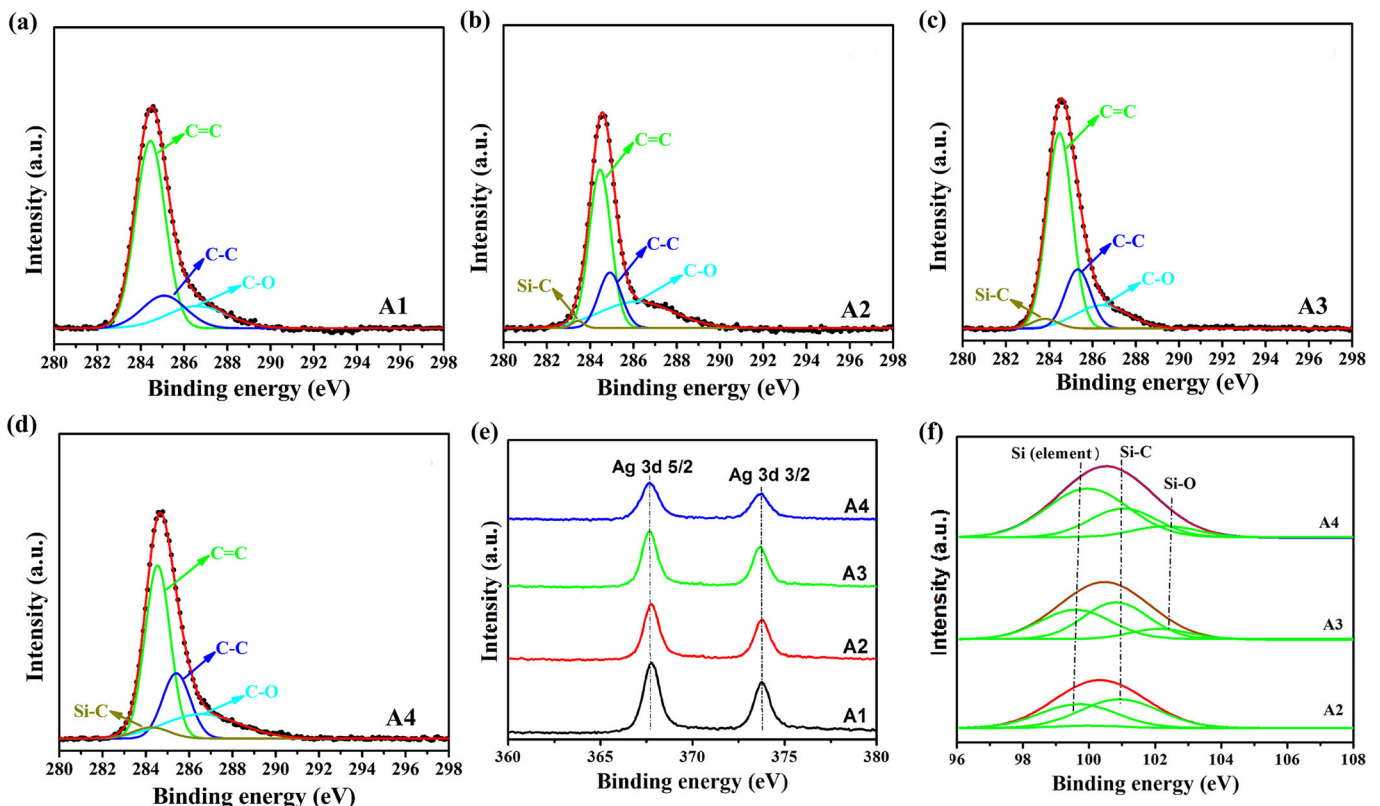


Figure 1. XPS fine spectra and the peak deconvolutions of the composite films: (a) C 1s in A1, (b) C 1s in A2, (c) C 1s in A3, (d) C 1s in A4, (e) Ag 3d, and (f) Si 2p.

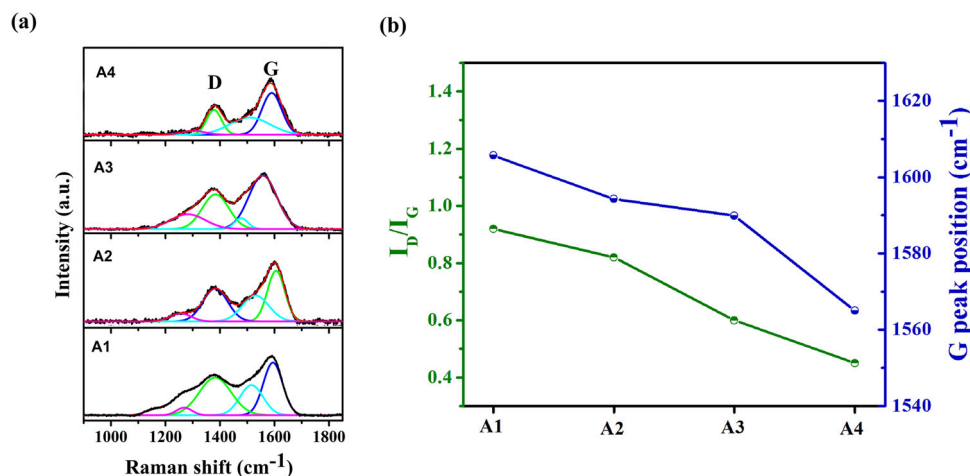


Figure 2. (a) Raman spectra and corresponding peak deconvolution and (b) I_D/I_G ratio and G peak position of the composite films.

indicates negligible differences in the state of Ag bonding in the films. Because the distance between the Ag $3d_{5/2}$ and Ag $3d_{3/2}$ peaks is 6.0 eV, it may be inferred that the Ag species incorporated in the films are in metallic form (25). The Si 2p spectra shown in Fig. 1f were fitted with Gaussian distributions centered at 99.6, 100.9, and 102.4 eV, assigned to Si, Si-C, and Si-O bonds, respectively. The small Si-O peak is attributed to physical adsorption of oxygen from the ambient. Thus, it may be inferred that the Si in the film mainly existed as free Si atoms and Si bonded to C. Interestingly, the peak assigned to Si atoms intensified with the decrease in substrate rotational speed. This may be associated with the rejection of excess Si atoms from Si-rich regions during the formation of crystalline SiC, resulting in the formation of noncrystalline Si regions around SiC grains close to the film surface (26).

Figure 2a shows Raman spectra of Si/Ag/a-C:H films including deconvolution peaks. The G peak centered at $\sim 1590 \text{ cm}^{-1}$ is due to in-plane stretching of sp^2 -bonded C atoms existing in olefinic chains and aromatic rings, and the D peak centered at $\sim 1350 \text{ cm}^{-1}$ is due to the breathing mode (out-of-plane stretching) of sp^2 -bonded C atoms existing only in the aromatic rings (27). The peaks centered at ~ 1514 and $\sim 1267 \text{ cm}^{-1}$ are due to the stretching mode of C=C bonds and the symmetric rocking *cis* double bond δ (=C-H) (28). The D-to-G peak intensity ratio, I_D/I_G , is commonly used to interpret structural changes in carbon materials. Because the G peak is due to all of the sp^2 sites and the D peak is only due to the sixfold rings, I_D/I_G decreases with decreasing number of rings per cluster and increasing fraction of chain groups. Thus, a high I_D/I_G ratio (and the shift of G peak toward higher wavenumbers) usually indicates a decrease in fourfold coordinated carbon atoms (29). Figure 2b indicates that both I_D/I_G and G peak position decreased monotonically with increasing Si content, suggesting a decrease in sp^2 atomic carbon hybridization with increasing Si content. The decrease in I_D/I_G may also indicate a decrease in graphite cluster size, whereas the downshift of the G peak position may be related to a decrease in film stress. Because the Si is more stable under sp^3 hybridization and prefers 3D formations, it can interrupt the C=C bonds,

inhibiting the formation of sp^2 carbon hybridization (30). Moreover, higher Si content leads to the formation of more Si-C because of positively charged Si and negatively charged C (31). The negatively charged C is more likely to attract and bond with H. The formation of Si-C bonds can increase the internal stress in the film and break the carbon rings, producing dangling C bonds in the chains that may bond with other positive particles in the matrix (including Si and H) to increase the content of sp^3 C-C bonding. The sharpening and downshifting of the G peak is likely due to the increase of sp^3 content and sp^2 bond angle disordering.

XRD spectra revealing the composition of the fabricated Si/Ag/a-C:H films are shown in Fig. 3. All patterns have four peaks assigned to Ag. The spectra also show the existence of SiC (111) and SiC (200) planes. The relative intensity of the SiC diffraction peaks demonstrates a gradual increase with Si content, indicating an increasing volume fraction of SiC crystals (32). The existence of Si (111) and Si (220) peaks only in the spectra of the films containing 8.2 and 10.98 at% Si (films A3 and A4, respectively) indicate the presence of silicon crystals. The XRD results shown in Fig. 3 are consistent with the XPS results shown in Fig. 1.

The FTIR spectroscopy results shown in Fig. 4 provide insight into the composition of hydrocarbon nanochains (33). The absorption peaks at ~ 784 and ~ 890 – 950 cm^{-1} are attributed to the vibration of Si-C mode (34). The absorption peak at ~ 1064 – 1100 cm^{-1} corresponds to the Si-O stretching vibration. The peaks in the range of 2700 – 3100 cm^{-1} can be fitted with Gaussian distributions centered at 2860, 2955, and 2925 cm^{-1} , corresponding to the stretching vibration of sp^3 CH₃, sp^3 CH, and sp^3 CH₂, respectively (35). The gradual increase in the intensity of the peak at $\sim 784 \text{ cm}^{-1}$ with increasing Si content indicates a corresponding increase in SiC concentration. (If both samples are of identical material and it is a transmission measurement, then usually it means either that the concentration or the path length is higher in one of the samples. For transmission spectroscopy, the intensity of absorption is described by the Beer-Lambert law.) The peak between 1376 and 1460 cm^{-1} that is visible only in the spectrum of the Ag/a-C:H film is assigned to in-phase deformation vibration of sp^3 CH₃ and indicates a higher CH₃ content for this film (36).

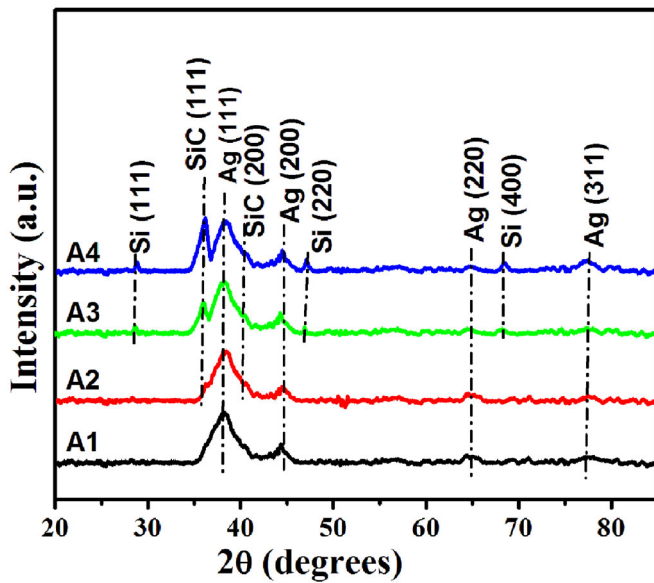


Figure 3. XRD patterns of the composite films.

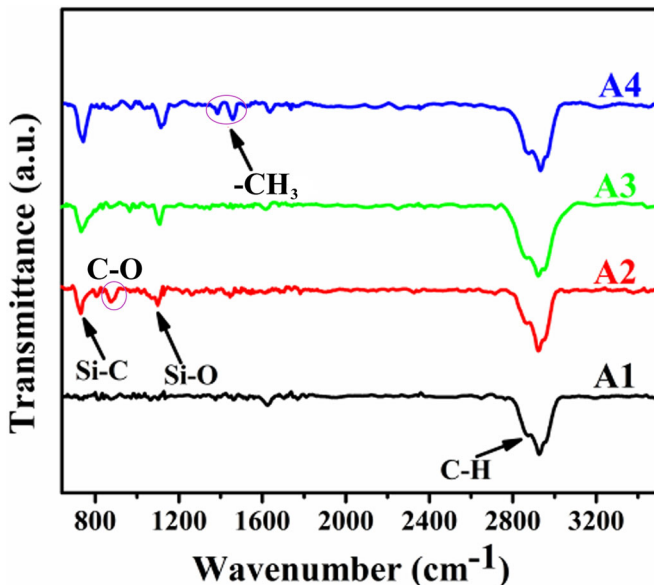


Figure 4. FTIR spectra of the composite films.

The peak centered at $\sim 876\text{ cm}^{-1}$ is assigned to the C-O stretching mode and exists only in the spectrum of film A2, which has the lowest Si content (4.42 at%). There is no evidence of Si-H bonding in any of the FTIR spectra, most likely due to the metal-like and positively charged Si in the Si-C network structure that repelled the H in the film.

Film surface morphology

Figure 5 shows representative AFM images of film surface morphologies. All of the film surfaces exhibited granulated topographies with nanoparticle density and size increasing with Si content. This is also indicated by the gradual increase in RMS roughness from 3.26 to 4.61 nm with Si content increasing from 0 to 10.98 at%. This trend can be explained by considering the film growth process. A critical feature of film deposition is the effect of energetic ions impinging on the growing film surface. The momentum

transferred by bombarding ions to the film surface enhances the mobility and diffusion of surface atoms and promotes the removal of asperities, thereby contributing to the growth of a smoother film (37). However, the decrease in substrate rotational speed resulted in longer time intervals between energetic ion bombardments. This explains the slight increase in film surface roughness with the increase in Si content in the range of 0–10.98 at%. The RMS roughness is most widely used and accurately reflects the contact conditions during sliding. The differences in the RMS roughness indicate the different numbers of asperities on the surface and thus the different friction and wear behaviors.

Mechanical properties

Table 2 gives the hardness H and elastic modulus E of the deposited films. The relatively low hardness and elastic modulus of all films is attributed to the doped Ag as a locally independent unit, which is isolated by the amorphous carbon matrix and bad for the overall connectivity of the carbon network. However, the incorporation of Si improved the mechanical properties significantly, most profoundly the film hardness, presumably due to the increased density of sp^3 C-C and Si-C bonds in the a -C:H matrix caused by Si and the formation of SiC nanocrystals in the carbon matrix that provided a hardening effect. The nanocrystalline/amorphous structure of the films does not favor the operation of dislocation sources and can restrain existing dislocations in adjacent nanocrystalline phases with different elastic constants (38).

The critical contact load at yielding P_Y of an asperity microcontact with a mean effective radius of curvature R is given by (39)

$$P_Y = \frac{9\pi^3}{16} c^3 R^3 Y \left(\frac{E^*}{Y} \right)^{-2}, \quad [1]$$

where $c = 1.08$ (von Mises yield criterion), Y is the yield strength of the film, and E^* is the effective elastic modulus, which for a rigid indenter is equal to $E/(1 - \nu^2)$, where E and ν are the elastic modulus and Poisson's ratio of the film, respectively. Considering the proportionality between hardness and yield strength—that is, $H = mY$ (40)—and the negligible effect of Si addition on Poisson's ratio, Eq. [1] can be modified to obtain the dimensionless yield load P_Y at an average-size asperity microcontact, given by

$$P_Y = \frac{16(1 - \nu^2)m^3 P_Y}{9\pi^3 c^3 R^3} = \frac{H^3}{E^2}. \quad [2]$$

Equation [2] indicates that the surface resistance to yielding (and, in turn, mechanical wear) increases with the H^3/E^2 ratio. Table 2 shows that H^3/E^2 increases significantly with Si content, implying that Si/Ag/ a -C:H nanocomposite films with higher Si content should exhibit better tribomechanical properties.

Tribological properties

Figure 6 shows representative friction coefficient results of the deposited films. Among the four film compositions

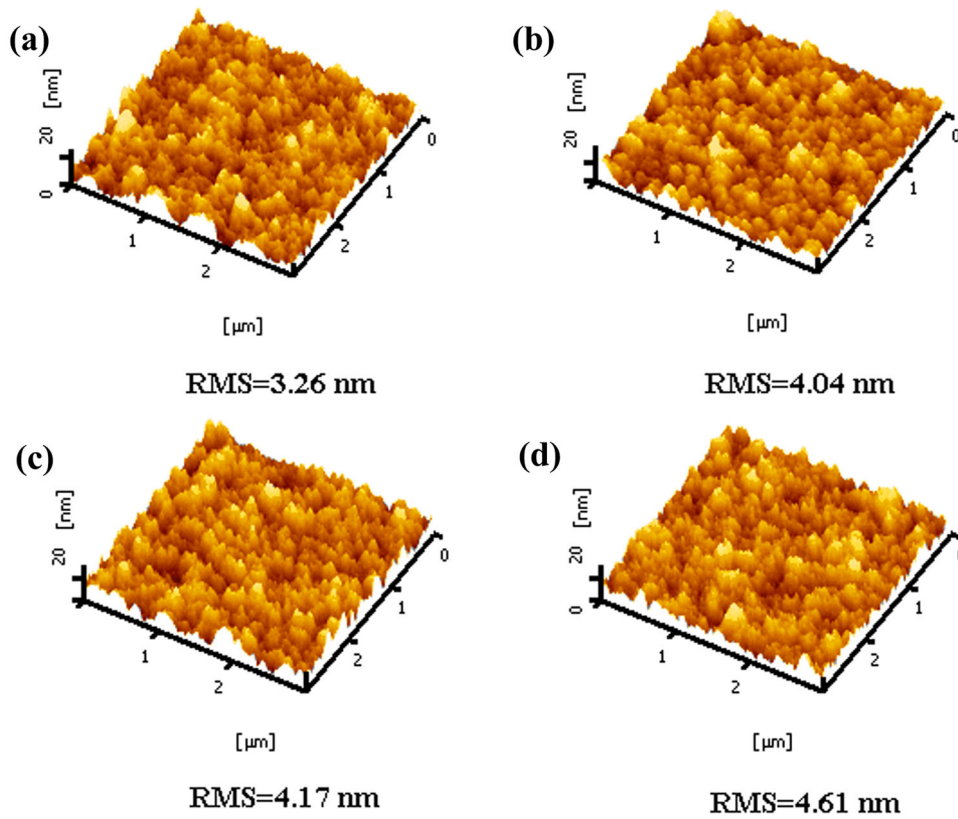


Figure 5. AFM images of the composite films: (a) A1, (b) A2, (c) A3, and (d) A4.

Table 2 Hardness (H), elastic modulus (E), and relative values of the composite films.

Sample	A1	A2	A3	A4
Hardness (GPa)	1.090	1.830	2.315	2.68
Elastic modulus (GPa)	16.55	15.60	18.25	19.20
H^3/E^2	0.005	0.025	0.037	0.052
H/E	0.066	0.117	0.127	0.140

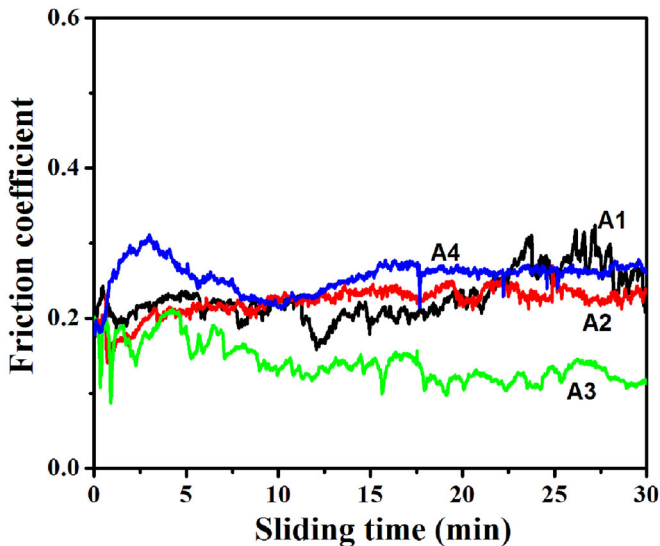


Figure 6. Coefficient of friction versus sliding time curves of the composite films in air.

investigated, the Si/Ag/*a*-C:H film with 8.2 at% Si shows the lowest steady-state friction coefficient (~ 0.15). All other films exhibit more fluctuating and higher friction coefficients in the

range of ~ 0.22 – 0.3 . The relatively large fluctuations in friction coefficient are usually indicative of more extensive surface damage (wear) and the entrapment of greater amounts of wear debris at the sliding interface, resulting in abrupt changes in the real contact area and, in turn, the magnitude of the friction force. Indeed, the foregoing is supported by the SEM images of worn film surfaces and corresponding steel ball surfaces shown in Fig. 7. The sliding pair including the Si/Ag/*a*-C:H film with 8.2 at% Si (film A3) demonstrates the best wear characteristics overall. All other sliding pairs show more pronounced and wider wear scars on the film surfaces and significantly more wear and material transfer on the steel surfaces. The mean friction coefficient and wear rate of all of the composite films are given in Fig. 8, which indicates that there is an optimum Si content for best tribological performance.

It is known that the microstructure of carbon films containing Si is characterized by soft and ductile phases, which improve film adhesion to the substrate and film toughness, and that Ag acts as a solid lubricant to decrease sliding friction (41). The low friction coefficient and wear rate of Si/Ag/*a*-C:H films are attributed to the high density of grain boundaries in the nanocrystal SiC phase that prevent crack growth by grain boundary diffusion and/or sliding (42). Interestingly, the differences in frictional behaviors of the films are thought to be the result of a combination of intrinsic and environmental factors, including H/E ratio, surface roughness, and lubricating phase. A high H/E ratio has been reported to correlate with high wear resistance (43, 44). A rough surface is more conducive to high friction and more wear damage. Because rough surface contact is mostly confined to asperity microcontacts that act as stress raisers, film

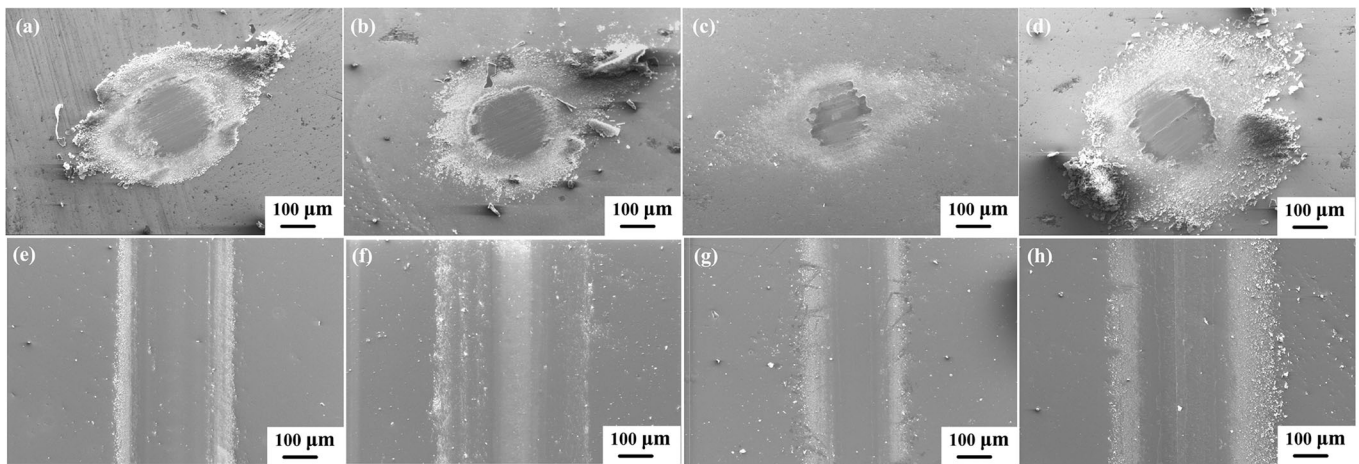


Figure 7. SEM images of the worn surfaces of the composite films and the corresponding counterpart ball: (a), (e) A1; (b), (f) A2; (c), (g) A3; and (d), (h) A4.

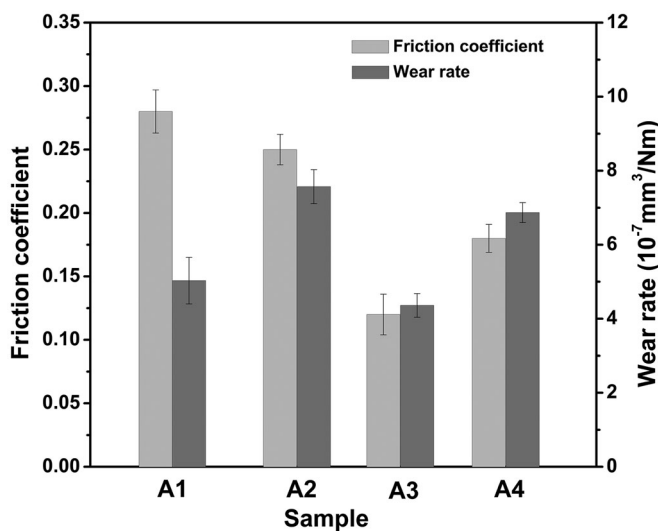


Figure 8. Mean friction coefficients and wear rates of the composite films.

scratching and wear are enhanced, resulting in higher sliding friction and wear rate. A higher Ag content in the film can maintain low shear strength at the counterface. All of these reasons explain the overall better tribological performance of the Si/Ag/*a*-C:H film containing 8.2 at% Si. Because the increase in Si is intertwined with an increase in the hard and abrasive SiC phase, increasing the Si content beyond 8.2 at% (e.g., film A4) not only increased the surface roughness but also the abrasiveness of the film due to the formation of hard SiC particles that enhanced abrasion of the steel countersurface, as evidenced from the SEM images of worn surfaces shown in Figs. 7d and 7h.

Conclusions

Films consisting of *a*-C:H, Ag, and Si were synthesized by magnetron sputtering and their composition, microstructure, and mechanical/tribological properties were examined. The purpose of incorporating Si in the films was to improve the film properties. The Si content of the films was varied by controlling the substrate rotational speed during deposition.

The incorporation of Si in the film microstructure increased the contents of sp^3 C, sp^3 CH, and sp^3 CH₂ and slightly the film surface roughness. The increase in strength of the films containing Si is attributed to the formation of a hard SiC phase and the connectivity of Si with the *a*-C:H matrix. The results of this study reveal the existence of an optimum Si content resulting in the best mechanical and tribological performance, which correlates with the existence of high sp^3 C and more SiC particles in the film and, thus, a relatively high H^3/E^2 ratio and low surface roughness.

Funding

The authors are grateful to the National Natural Science Foundation of China (Grant Nos. 51505318, 51801133, 51671140), Science and Technology Major Project of Shanxi (20181102013), Shanxi Provincial Youth Fund (201801D221135), “1331 Project” Engineering Research Center of Shanxi (PT201801), and China Scholarship Council for financial support.

ORCID

Kyriakos Komvopoulos  <http://orcid.org/0000-0001-9418-1567>

References

- (1) Martinez-Martinez, D. and De Hosson, J. Th. M. (2014), “On the Deposition and Properties of DLC Protective Coatings on Elastomers: A Critical Review,” *Surface and Coatings Technology*, **258**, pp 677–690.
- (2) Erdemir, A. (2001), “The Role of Hydrogen in Tribological Properties of Diamond-Like Carbon,” *Surface and Coatings Technology*, **146–147**, pp 292–297.
- (3) Corbella, C., Vives, M., Pinyol, A., Bertran, E., Canal, C., Polo, M. C., and Andújar, J. L. (2004), “Preparation of Metal (W, Mo, Nb, Ti) Containing *a*-C:H Films by Reactive Magnetron Sputtering,” *Surface and Coatings Technology*, **177–178**, pp 409–414. doi:10.1016/j.surfcoat.2003.09.017
- (4) Gayathri, S., Kumar, N., Krishnan, R., Ravindran, T. R., Dash, S., Tyagi, A. K., Raj, B., and Sridharan, M. (2012), “Tribological Properties of Pulsed Laser Deposited DLC/TM (TM = Cr, Ag, Ti and Ni) Multilayers,” *Tribology International*, **53**, pp 87–97. doi:10.1016/j.triboint.2012.04.015

- (5) Li, X., Sun, L., Guo, P., Ke, P., and Wang, A. (2016), "Structure and Residual Stress Evolution of Ti/Al, Cr/Al or W/Al Co-Doped Amorphous Carbon Nanocomposite Films: Insights from Ab Initio Calculations," *Materials & Design*, **89**, pp 1123–1129. doi:10.1016/j.matdes.2015.10.106
- (6) Singh, V., Jiang, J. C., and Meletis, E. I. (2005), "Cr-Diamondlike Carbon Nanocomposite Films: Synthesis, Characterization and Properties," *Thin Solid Films*, **489**, pp 150–158. doi:10.1016/j.tsf.2005.04.104
- (7) Dai, W. and Wang, A. (2011), "Deposition and Properties of Al-Containing Diamond-Like Carbon Films by a Hybrid Ion Beam Sources," *Journal of Alloys and Compounds*, **509**, pp 4626–4631. doi:10.1016/j.jallcom.2011.01.132
- (8) Wu, Y., Chen, J., Li, H., Ji, L., Ye, Y., and Zhou, H. (2013), "Preparation and Properties of Ag/DLC Nanocomposite Films Fabricated by Unbalanced Magnetron Sputtering," *Applied Surface Science*, **284**, pp 165–170. doi:10.1016/j.apsusc.2013.07.074
- (9) Bociaga, D., Komorowski, P., Batory, D., Szymanski, W., Olejnik, A., Jastrzebski, K., and Jakubowski, W. (2015), "Silver-Doped Nanocomposite Carbon Coatings (Ag-DLC) for Biomedical Applications—Physiochemical and Biological Evaluation," *Applied Surface Science*, **355**, pp 388–397. doi:10.1016/j.apsusc.2015.07.117
- (10) Manninen, N. K., Galindo, R. E., Carvalho, S., and Cavaleiro, A. (2015), "Silver Surface Segregation in Ag-DLC Nanocomposite Coatings," *Surface and Coatings Technology*, **267**, pp 90–97. doi:10.1016/j.surfcoat.2014.12.029
- (11) Cloutier, M., Turgeon, S., Busby, Y., Tatoulian, M., Pireaux, J.-J., and Mantovani, D. (2016), "Controlled Distribution and Clustering of Silver in Ag-DLC Nanocomposite Coatings Using a Hybrid Plasma Approach," *ACS Applied Materials & Interfaces*, **8**, pp 21020–21027. doi:10.1021/acsami.6b06614
- (12) Hlíděk, P., Biederman, H., Choukourou, A., and Slavinská, D. (2008), "Behavior of Polymeric Matrices Containing Silver Inclusions, 1—Review of Adsorption and Oxidation of Hydrocarbons on Silver Surfaces/Interfaces as Witnessed by FT-IR Spectroscopy," *Plasma Processes and Polymers*, **5**, pp 807–824. doi:10.1002/ppap.200800083
- (13) Drábik, M., Pešička, J., Biederman, H., and Hegemann, D. (2015), "Long-Term Aging of Ag/a-C:H:O Nanocomposite Coatings in Air and in Aqueous Environment," *Science and Technology of Advanced Materials*, **16**, pp 025005. doi:10.1088/1468-6996/16/2/025005
- (14) Li, X., Guo, P., Sun, L., Zuo, X., Zhang, D., Ke, P., and Wang, A. (2017), "Ti/Al Co-Doping Induced Residual Stress Reduction and Bond Structure Evolution of Amorphous Carbon Films: An Experimental and Ab Initio Study," *Carbon*, **111**, pp 467–475. doi:10.1016/j.carbon.2016.10.033
- (15) Liu, X., Yang, J., Hao, J., Zheng, J., Gong, Q., and Liu, W. (2012), "A Near-Frictionless and Extremely Elastic Hydrogenated Amorphous Carbon Film with Self-Assembled Dual Nanostructure," *Advanced Materials*, **24**, pp 4614–4617. doi:10.1002/adma.201200085
- (16) Wilhelmsson, O., Räsander, M., Carlsson, M., Lewin, E., Sanyal, B., Wiklund, U., Eriksson, O., and Jansson, U. (2007), "Design of Nanocomposite Low-Friction Coatings," *Advanced Functional Materials*, **17**, pp 1611–1616. doi:10.1002/adfm.200600724
- (17) Pang, X., Hao, J., Wang, P., Xia, Y., and Liu, W. (2011), "Effects of Bias Voltage on Structure and Properties of TiAl-Doped a-C:H Films Prepared by Magnetron Sputtering," *Surface and Interface Analysis*, **43**, pp 677–682. doi:10.1002/sia.3501
- (18) Zhao, F., Li, H. X., Ji, L., Mo, Y. F., Quan, W. L., Du, W., Zhou, H. D., and Chen, J. M. (2009), "Superlow Friction Behavior of Si-Doped Hydrogenated Amorphous Carbon Film in Water Environment," *Surface and Coatings Technology*, **203**, pp 981–985. doi:10.1016/j.surfcoat.2008.09.025
- (19) Ong, S.-E., Zhang, S., Du, H., Too, H.-C., and Aung, K.-N. (2007), "Influence of Silicon Concentration on the Haemocompatibility of Amorphous Carbon," *Biomaterials*, **28**, pp 4033–4038. doi:10.1016/j.biomaterials.2007.05.031
- (20) Kolodziejczyk, L., Szymanski, W., Batory, D., and Jedrzejczak, A. (2016), "Nanotribology of Silver and Silicon Doped Carbon Coatings," *Diamond and Related Materials*, **67**, pp 8–15. doi:10.1016/j.diamond.2015.12.010
- (21) Swiatek, L., Olejnik, A., Grabarczyk, J., Jedrzejczak, A., Sobczyk-Guzenda, A., Kaminska, M., Jakubowski, W., Szymanski, W., and Bociaga, D. (2016), "Multi-Doped Diamond Like-Carbon Coatings (DLC-Si/Ag) for Biomedical Applications Fabricated Using the Modified Chemical Vapour Deposition Method," *Diamond and Related Materials*, **67**, pp 54–62. doi:10.1016/j.diamond.2016.03.005
- (22) Duta, L., Ristoscu, C., Stan, G. E., Husanu, M. A., Besleaga, C., Chifriuc, M. C., Lazar, V., Bleotu, C., Miculescu, F., Mihailescu, N., Axente, E., Badiceanu, M., Bociaga, D., and Mihailescu, I. N. (2018), "New Bio-active, Antimicrobial and Adherent Coatings of Nanostructured Carbon Double-Reinforced with Silver and Silicon by Matrix-Assisted Pulsed Laser Evaporation for Medical Applications," *Applied Surface Science*, **441**, pp 871–883. doi:10.1016/j.apsusc.2018.02.047
- (23) Wang, L. J., Zhang, F., Fong, A., Lai, K. M., Shum, P. W., Zhou, Z. F., Gao, Z. F., and Fu, T. (2018), "Effects of Silver Segregation on Sputter Deposited Antibacterial Silver-Containing Diamond-Like Carbon Films," *Thin Solid Films*, **650**, pp 58–64. doi:10.1016/j.tsf.2018.02.015
- (24) Nöthe, M., Breuer, U., Koch, F., Penkalla, H. J., Rehbach, W. P., and Bolt, H. (2001), "Investigation of the Structure and Properties of a-C:H Coatings with Metal and Silicon Containing Interlayers," *Applied Surface Science*, **179**, pp 122–128.
- (25) Mathpal, M. C., Kumar, P., Kumar, S., Tripathi, A. K., Singh, M. K., Prakash, J., and Agarwal, A. (2015), "Opacity and Plasmonic Properties of Ag Embedded Glass Based Metamaterials," *RSC Advances*, **5**, pp 12555–12562. doi:10.1039/C4RA14061C
- (26) Takeshita, T., Kurata, Y., and Hasegawa, S. (1992), "Bonding Properties of Glow-Discharge Polycrystalline and Amorphous Si-C Studied by X-ray Diffraction and X-ray Photoelectron Spectroscopy," *Journal of Applied Physics*, **71**, pp 5395–5400. doi:10.1063/1.350561
- (27) Irmer, G. and Dörner-Reisel, A. (2005), "Micro-Raman Studies on DLC Coatings," *Advanced Engineering Materials*, **7**, pp 694–705. doi:10.1002/adem.200500006
- (28) Rebelo, S. L. H., Guedes, A., Szeftczyk, M. E., Pereira, A. M., Araújo, J. P., and Freire, C. (2016), "Progress in the Raman Spectra Analysis of Covalently Functionalized Multiwalled Carbon Nanotubes: Unraveling Disorder in Graphitic Materials," *Physical Chemistry Chemical Physics*, **18**, pp 12784–12796. doi:10.1039/c5cp06519d
- (29) Zhang, S., Zeng, X. T., Xie, H., and Hing, P. (2000), "A Phenomenological Approach for the I_d/I_g Ratio and sp^3 Fraction of Magnetron Sputtered a-C Films," *Surface and Coatings Technology*, **123**, pp 256–260. doi:10.1016/S0257-8972(99)00523-X
- (30) Zhao, F., Li, H. X., Ji, L., Mo, Y. F., Quan, W. L., Zhou, H. D., and Chen, J. M. (2009), "Structural, Mechanical and Tribological Characterizations of a-C:H:Si Films Prepared by a Hybrid PECVD and Sputtering Technique," *Journal of Physics D: Applied Physics*, **42**, pp 165407. doi:10.1088/0022-3727/42/16/165407
- (31) Mavrandonakis, A., Froudakis, G. E., Schnell, M., and Mühlhäuser, M. (2003), "From Pure Carbon to Silicon-Carbon Nanotubes: An Ab-Initio Study," *Nano Letters*, **3**, pp 1481–1484. doi:10.1021/nl0343250
- (32) Ji, L., Wu, Y., Li, H., Song, H., Liu, X., Ye, Y., Chen, J., Zhou, H., and Liu, L. (2015), "The Role of Trace Ti Concentration on the Evolution of Microstructure and Properties of Duplex

- Doped Ti(Ag)/DLC Films,” *Vacuum*, **115**, pp 23–30. doi: [10.1016/j.vacuum.2015.01.023](https://doi.org/10.1016/j.vacuum.2015.01.023)
- (33) Liu, H., Huang, Z., Huang, J., Fang, M., Liu, Y.-g., and Wu, X. (2014), “Thermal Evaporation Synthesis of SiC/SiO_x Nanochain Heterojunctions and Their Photoluminescence Properties,” *Journal of Materials Chemistry C*, **2**, pp 7761–7767. doi:[10.1039/C4TC01391C](https://doi.org/10.1039/C4TC01391C)
- (34) Lenza, R. F. S. and Vasconcelos, W. L. (2001), “Structural Evolution of Silica Sols Modified with Formamide,” *Materials Research*, **4**, pp 175–179. doi:[10.1590/S1516-14392001000300006](https://doi.org/10.1590/S1516-14392001000300006)
- (35) Ristein, J., Stief, R. T., Ley, L., and Beyer, W. (1998), “A Comparative Analysis of *a*-C:H by Infrared Spectroscopy and Mass Selected Thermal Effusion,” *Journal of Applied Physics*, **84**, pp 3836–3847. doi:[10.1063/1.368563](https://doi.org/10.1063/1.368563)
- (36) Liao, M., Feng, Z., Chai, C., Yang, S., Liu, Z., and Wang, Z. (2002), “Violet/Blue Emission from Hydrogenated Amorphous Carbon Films Deposited from Energetic CH₃⁺ Ions and Ion Bombardment,” *Journal of Applied Physics*, **91**, pp 1891–1893. doi: [10.1063/1.428086](https://doi.org/10.1063/1.428086)
- (37) Zheng, W. T., Hellgren, N., Sjöström, H., and Sundgren, J.-E. (1998), “Characterization of Carbon Nitride Thin Films Deposited by Reactive D.C. Magnetron Sputtering on Various Substrate Materials,” *Surface and Coatings Technology*, **100–101**, pp 287–290. doi:[10.1016/S0257-8972\(97\)00634-8](https://doi.org/10.1016/S0257-8972(97)00634-8)
- (38) Voevodin, A. A. and Zabinski, J. S. (2000), “Supertough Wear-Resistant Coatings with ‘Chameleon’ Surface Adaptation,” *Thin Solid Films*, **370**, pp 223–231. doi:[10.1016/S0040-6090\(00\)00917-2](https://doi.org/10.1016/S0040-6090(00)00917-2)
- (39) Song, Z. and Komvopoulos, K. (2014), “An Elastic–Plastic Analysis of Spherical Indentation: Constitutive Equations for Single-Indentation Unloading and Development of Plasticity Due to Repeated Indentation,” *Mechanics of Materials*, **76**, pp 93–101. doi: [10.1016/j.mechmat.2014.05.005](https://doi.org/10.1016/j.mechmat.2014.05.005)
- (40) Tabor, D. (1948), “A Simple Theory of Static and Dynamic Hardness,” *Proceedings of the Royal Society of London: Series A*, **192**, pp 247–274.
- (41) Manninen, N. K., Ribeiro, F., Escudeiro, A., Polcar, T., Carvalho, S., and Cavaleiro, A. (2013), “Influence of Ag Content on Mechanical and Tribological Behavior of DLC Coatings,” *Surface and Coatings Technology*, **232**, pp 440–446. doi:[10.1016/j.surfcoat.2013.05.048](https://doi.org/10.1016/j.surfcoat.2013.05.048)
- (42) Voevodin, A. A., Zabinski, J. S., and Muratore, C. (2005), “Recent Advances in Hard, Tough, and Low Friction Nanocomposite Coatings,” *Tsinghua Science and Technology*, **10**, pp 665–679. doi:[10.1016/S1007-0214\(05\)70135-8](https://doi.org/10.1016/S1007-0214(05)70135-8)
- (43) Leyland, A. and Matthews, A. (2000), “On the Significance of the H/E Ratio in Wear Control: A Nanocomposite Coating Approach to Optimised Tribological Behaviour,” *Wear*, **246**, pp 1–11.
- (44) Dragatogiannis, D. A., Koumoulos, E., Ellinas, K., Tserepi, A., Gogolides, E., and Charitidis, C. A. (2015), “Nanoscale Mechanical and Tribological Properties of Plasma Nanotextured COP Surfaces with Hydrophobic Coatings,” *Plasma Processes and Polymers*, **12**, pp 1271–1283. doi:[10.1002/ppap.201500023](https://doi.org/10.1002/ppap.201500023)